Chemical Engineering Journal 425 (2021) 131456

Contents lists available at ScienceDirect

Chemical Engineering Journal

journal homepage: www.elsevier.com/locate/cej

Water-driven $CsPbBr_3$ nanocrystals and poly(methyl methacrylate)-$CsPbBr_3$ nanocrystal films with bending-endurable photoluminescence

Xiaobing Tang [a], Nadeesha Lakmali Kothalawala [b], Yulin Zhang [a], Dali Qian [c], Doo Young Kim [b], Fuqian Yang [a,*]

[a] Materials Program, Department of Chemical and Materials Engineering, University of Kentucky, Lexington, KY 40506, USA
[b] Department of Chemistry, University of Kentucky, Lexington, KY 40506, USA
[c] Electron Microscopy Center, University of Kentucky, Lexington, KY 40506, USA

ARTICLE INFO

Keywords:
Perovskite nanocrystal
Water
Dual color emission
Bending-endurable backlight films

ABSTRACT

Perovskite nanocrystals are regarded as next-generation functional materials for display applications, especially for flexible liquid crystal displays (LCDs). As a potential component of flexible LCD backlights, perovskite nanocrystal films are facing a challenge issue of deformation-induced shift of photoluminescence, leading to an image distortion. To date, most synthesis methods have involved the use of organic solvent in precursor solutions, such as N,N-dimethylformamide and dimethyl sulfoxide, which poses a potential threat to the environment, health and security. In this work, we demonstrate the feasibility to produce microsized $CsPbBr_3$ crystals with deionized water as the precursor solvent via an environmental-friendly and cost-efficient approach and $CsPbBr_3$ nanocrystals with green (~522 nm) and blue (~493 nm) emissions from the microsized $CsPbBr_3$ crystals in toluene under sonication. The blue-emitting nanocrystals exhibit a photoluminescence (PL) quantum yield of 80%, much larger than 61.4% of the $CsPbBr_3$ nanocrystals made by an anti-solvent method; the green-emitting nanocrystals exhibit better stability than those made by the antisolvent method over 9 days. Using the green-emitting $CsPbBr_3$ nanocrystals, we prepare a bilayer structure with a poly(methyl methacrylate)-$CsPbBr_3$ nanocrystal film on a polyethylene terephthalate plate. The films exhibit bending-endurable photoluminescence, i.e. the wavelength of the PL peak remains unchanged, for local radius of curvature of the bilayer up to 10.07 mm under bending. This study opens a new avenue to potentially produce microsized perovskite crystals without harmful organic solvents and bending-endurable backlight films for the applications in flexible display.

1. Introduction

Semiconductor nanocrystals (NCs) with outstanding characteristics of color tunability and high quantum yield have promising applications in a variety of fields, including lighting and display [1–4], solar cells [5,6], bio-imaging [7,8], etc. To date, the most investigated NCs are cadmium-based chalcogenides NCs, whose further commercialization, however, has been hindered mainly by cost issue [9], associated with complex and expensive fabrication processes to form core-shell structure at high reaction temperatures, and structural stabilities [6,10,11].

Lead halide perovskite nanocrystals (PeNCs) with high brightness, wide color gamut, high color purity, high defect tolerance and a lower cost than the conventional cadmium-based chalcogenides NCs have attracted great interest for their potential applications in next-generation high-performance lighting [12] and vivid color display [13]. The progress in the synthesis of PeNCs, including the combination with polymers [14], has led to rapid advancement in optoelectronic field [9,15–22], especially, NC-backlight embedded flexible LCD (NC-LCD) [23]. However, this technology is suffered from the image-distortion issues caused by local deformation in the NC-based backlight films [24–28], which has been a burning question needed to be solved.

There are many efforts on the strain effect on the PL (photoluminescence) characteristics of perovskites. For example, Li et al. [24] reported that compressive strain introduced during the cooling caused red shift of the PL peak and reduced the stability of the $CsPbBr_3$ thin-film crystals. Zhong et al. [28] observed a remarkable PL shift of $CsPbBr_3$ quantum dots under hydrostatic pressure. It needs to be pointed out that there are few reports focusing on the effects of bending and tensile deformation. All the reported findings have revealed the PL shift of perovskites under mechanical deformation, which is detrimental to the

* Corresponding author.
E-mail address: fuqian.yang@uky.edu (F. Yang).

https://doi.org/10.1016/j.cej.2021.131456
Received 13 May 2021; Received in revised form 17 July 2021; Accepted 19 July 2021
Available online 8 August 2021

applications in high-quality display. There is a great need to develop backlight materials with deformation-endurable PL characteristics.

Currently, most studies for the synthesis of PeNCs have been concentrated on high temperature injection (HI) [29] and room-temperature antisolvent processes [9,30], which exhibit critical drawbacks. The vacuuming of a rection vessel, when alternated with an inert gas inflation, makes HI an intricate, time consuming and high-cost process. The gas inflation can cause a suck-back of liquid/solution, which is extremely detrimental to the system and dangerous during the synthesis. These methods also pose a significant threat to the environment, since the solvents used for the preparation of precursor solutions, such as octadecene (ODE) [29], dimethyl formamide (DMF) [9,30,31], dimethyl sulfoxide (DMSO) [30,32] and so forth, are volatile-organic and toxic. Using environmentally benign solvents/liquids in the synthesis of PeNCs is the best option from the viewpoint of sustainability [32]. Note that Li et al [31]. reported an aqueous method to prepare PeNCs, of which the PL intensity maintained ~80% of the initial value after 1 week storage at room temperature, while it requires a complicated ice-water bath process and the use of DMF. Recently, Cao et al. [33] reported an approach for the synthesis of CsPbBr3 films via a two-step spin coating using water as solvent. However, the use of volatile, environmentally hazardous DMF in their work faded the "so-called" green-route method. Also, they did not discuss how the reaction led to the formation of CsPbBr3 films.

To address these challenges, we developed a green route to environmental-friendly synthesize inorganic $CsPbBr_3$ crystals of micro-sizes with deionized (DI) water instead of organic solvents for the first time and $CsPbBr_3$ PeNCs in toluene from the microsized $CsPbBr_3$ crystals under sonication. The hydrochromic properties of the $CsPbBr_3$ NCs were realized from the "reversible" transformation between a green luminescent $CsPbBr_3$ (emission wavelength of ~522 nm) and a non-luminescent Cs_4PbBr_6 in water. We derived blue-emitting $CsPbBr_3$ PeNCs (emission wavelength of ~493 nm) from the green-emitting $CsPbBr_3$ via a powerful ultrasonication and centrifugation at room temperature consequently. The $CsPbBr_3$ NCs prepared by the ultrasonication exhibited superior optical stability to those prepared by an anti-solvent method, which can be attributed to the reduced specific surface area (SBET) and trap state density of the NCs. Using the green-emitting $CsPbBr_3$ NCs, we prepared bilayer structures consisting of a poly(methyl methacrylate) (PMMA)-$CsPbBr_3$ NC film on a polyethylene terephthalate (PET) plate. The PMMA-$CsPbBr_3$ NC films exhibited superior optical stability without optical degradation over a period of 30 days and retained ~100% of the initial PL intensity. The bending deformation of the bilayer structure did not cause the PL shift of the PMMA-$CsPbBr_3$ NC films for the local radius of curvature of the bilayer up to 10.07 mm, corresponding to a tensile strain of 3.97% in the films, and after "full" recovery to the un-deformed configuration.

2. Experimental methods

2.1. Materials

CsBr (99.9%, Beantown Chemical), $PbBr_2$ (>98%, Strem Chemicals Inc.), N,N-dimethylformamide (DMF) (VWR), oleic acid (OA) (Ward's Science), oleylamine (OAm) (>50%, TCI America), toluene (VWR) and DI water were used in the synthesis of $CsPbBr_3$ NCs. All the chemicals were used as received without further purification.

2.2. Water-driven $CsPbBr_3$ NCs

The $CsPbBr_3$ NCs were derived from $CsPbBr_3$ powders via ultrasonication. For the preparation of $CsPbBr_3$ powders, placing CsBr and $PbBr_2$ in DI water at room temperature produced white precipitates (Cs_4PbBr_6 and $PbBr_2$). The white precipitates were coated on the surface of a glass substrate of 2.5×2.5 cm^2 by a blade coater to form a white-thin layer, as shown schematically in Fig. 1a. The glass with the white-thin

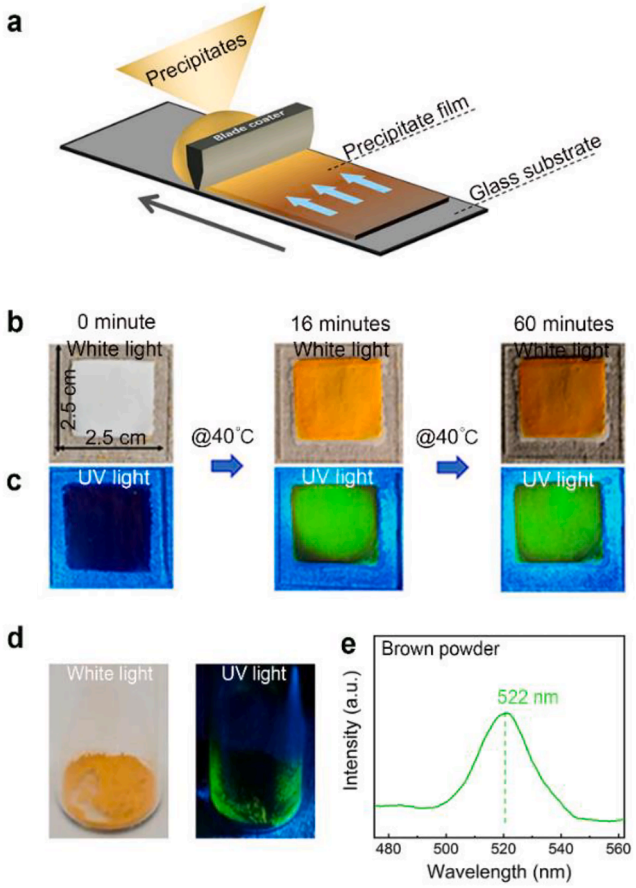

Fig. 1. Scheme for the preparation of $CsPbBr_3$ powders: (a) schematic for the preparation of a layer of $CsPbBr_3$ powders on a glass slide from white precipitates (Cs_4PbBr_6 and $PbBr_2$), (b) optical images showing the change of a white layer to a brown one under white light at two instants, (c) optical images corresponding to the ones in b under UV light of 365 nm, (d) optical images of brown powders under white light (left) and UV light of 365 nm (right), and (e) PL spectrum of the brown powders excited under of UV light of 365 nm.

layer was placed on a hot plate, heated to 40°C and maintained at 40°C for a certain time period (Fig. 1b). The white-thin layer after 16 min heating changed to a yellow-thin layer, which emitted green light under UV light (365 nm, same hereinafter). Further heating the coated thin layer for a total of 60 min led to the change of the white-thin layer to a brown-thin layer, which emitted green light (Fig. 1c). Such behavior is in sharp contrast to the nonluminous white one and suggests a phase transformation or the formation of new material during the heating.

The brown powders, as shown in Fig. 1d, were collected by scraping the brown film from the surface of the glass substrate. The PL spectrum of the brown powders exhibits a single PL peak centered at ~522 nm (Fig. 1e), confirming the formation of $CsPbBr_3$ [34]. Ultrasonicating the as-obtained brown powders in toluene for various durations in an ultrasonic bath (Reliance Sonic 550), we obtained $CsPbBr_3$ NCs.

2.3. Synthesis of $CsPbBr_3$ NCs by antisolvent method

Following the methods reported in the literature [9,30], we prepared $CsPbBr_3$ NCs by an antisolvent method. Briefly, a solution consisting of DMF (10 mL), OA (1 mL), OAm (0.5 mL), CsBr (0.4 mmol) and $PbBr_2$ (0.4 mmol) was stirred at 30°C overnight to form a precursor solution. 1 mL of the prepared precursor solution was quickly placed in toluene (10 mL) under vigorous stirring at 30°C to form $CsPbBr_3$ NCs.

2.4. Preparation of PMMA-NC films from water-driven $CsPbBr_3$ NCs and antisolvent-prepared $CsPbBr_3$ NCs

PMMA powders (Mw = 35000) (Fisher Scientific) were dissolved in toluene to form a PMMA solution of 0.02 g/ml in concentration. Purified $CsPbBr_3$ NCs made from the ultrasonication and antisolvent methods were added respectively into the as-prepared PMMA solution to obtain corresponding PMMA-NC solutions (0.32 g/ml). Coating the PMMA-NC solutions onto PET plates of $0.80\times6.66\times72.62$ mm^3 in dimensions led to the formation of corresponding PMMA-NC films of ~0.03 mm in thickness on PET plates.

2.5. Production yield of the water-driven $CsPbBr_3$ NCs

The sonication of a suspension consisting of 15.9439 g $CsPbBr_3$ powders, 50 μL OA, 25 μL OAm and 5 mL toluene in a glass vial for 100 min led to the production of green-emitting $CsPbBr_3$ NCs. The $CsPbBr_3$ NCs were dried on a hot plate at 40°C. The final weight of the $CsPbBr_3$ NCs was 15.5517 g. Using these weights, the production yield of the $CsPbBr_3$ NCs was calculated (Fig. S1 in Supplementary Information).

2.6. Materials characterization

XRD (X-ray diffraction) measurements were performed on an X-ray diffractometer (Siemens D500). The imaging of the $CsPbBr_3$ NCs/powders was carried out on an inverted confocal microscope (Leica SP8). TEM (transmission electron microscopy) and HRTEM (high resolution transmission electron microscopy) (Thermo-scientific Talos F200X TEM operated at an accelerating voltage of 200 kV) analyses were conducted to analyze the structures and morphologies of the $CsPbBr_3$ NCs. The brown $CsPbBr_3$ powders were further analyzed on an energy dispersive X-ray (EDX) spectroscope (Thermo-scientific Super-X System with four windowless silicon-drift-detectors (SDD) installed on a Talos F200X TEM). The PLQY and TCSPC measurements were carried out on a spectrofluorometer (FluoroMax-Plus-C) with an excitation wavelength of 390 nm.

2.7. PL and TCSPC (time correlated single photon counting) measurements

PL spectra were collected on a Horiba Scientific Fluoromax Plus-C fluorometer using 2 nm entrance and exit slits and an integration time of 0.1 s for both excitation and emission scans. PL decay measurements were performed using a DeltaHub™ high throughput TCSPC controller and a NanoLED-390 pulsed excitation source (excitation wavelength 393 ± 10 nm). TCSPC curves were collected at 425 and 465 nm emission with 5 nm bandpass at a repetition rate of 1 MHz over a measurement time of 200 ns. The instrument response function (IRF) was determined by measuring the scattering of the excitation source with a ludox sample. The fitting of decay curves was done using the Horiba Scientific decay analysis software DAS6.

2.8. UV-VIS absorption spectrum

UV-Vis absorption measurements were carried out on a Thermo Scientific Evolution 201 UV-Visible spectrophotometer. The samples were scanned in the wavelength range of 300–800 nm with a bandwidth of 1 nm and 0.1 s integration time.

2.9. PLQY (absolute photoluminescence quantum yield) measurements

PLQY measurements were carried out using an integrated sphere connected to the Horiba Scientific Fluoromax Plus-C fluorometer. The excitation wavelengths, which give the maximum emission, were used in the PLQY measurements. The parameters of 0.5 nm slit width and 0.1 s integration time were used. The PLQY calculations were done using the Horiba Scientific FluorEssence™ software.

2.10. PL measurement of the PMMA-NC films with and without bending

The bilayer structure was mechanically bent on a center open vise. The PL measurement of the the PMMA-NC films with and without bending was perfomed at various postions using a laser beam of 405 nm in wavelength. A reflective optical fiber was used. More detailed information on the bending state is given in Fig. S2 and Table S1 in Supplementary Information.

3. Results and discussion

The crystallographic structure of the white precipitates and brown powders shown in Fig. 1b were determined on an X-ray diffractometer (XRD) (Bruker D8). The XRD patterns are depicted in Fig. 2. The lower XRD pattern, which matches the standard JCPDS card (PDF#73-2478) and ICSD# 98-002-5124, indicates that the white precipitates are Cs_4PbBr_6 of hexagonal structure [34–37]; the middle XRD pattern, which matches the standard JCPDS card (PDF#72-7929), confirms that the brown powders are $CsPbBr_3$ of orthorhombic structure with small trace of Cs_4PbBr_6 and $PbBr_2$ (JCPDS card (PDF#85-0189)). The residuals of Cs_4PbBr_6 and $PbBr_2$ can be attributed to the incomplete reaction of Cs_4PbBr_6 with $PbBr_2$ to form $CsPbBr_3$. The elemental composition of the brown powders was further analyzed on an energy dispersive X-ray (EDX) (FEI Quanta 250 Features) and presented in Fig. S3 and Table S2 of Supplementary Information. The elemental ratio of Cs:Pb:Br is 16.42:17.78:65.80, which is compatible with the stoichiometry of $CsPbBr_3$ and in consistence to the XRD result.

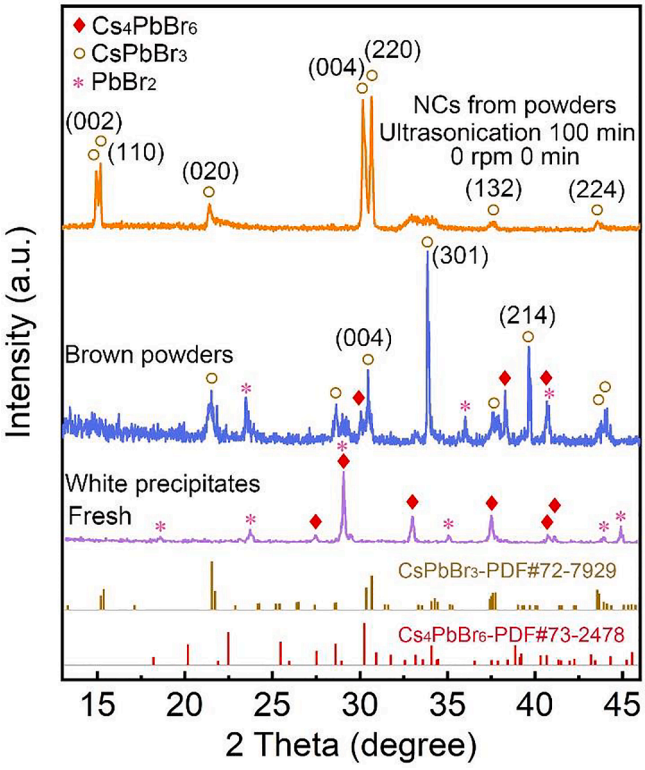

Fig. 2. XRD patterns of fresh white precipitates (purple curve), brown powders (blue curve) from fresh white precipitates heated at 40°C for 1 h, and $CsPbBr_3$ NCs (brown curve) from $CsPbBr_3$ brown powders by ultrasonication method for 100 min without centrifugation. The XRD patterns are well coincident with PDF card#73-2478 and ICSD# 98-002-5124 of Cs_4PbBr_6, PDF card#72-7929 of $CsPbBr_3$, and PDF card#85–0189 of $PbBr_2$, respectively. The XRD pattern (brown curve) of the $CsPbBr_3$ NCs is coincident well with PDF card#72–7929.

Using the Scherrer equation and the XRD pattern, we obtain the crystallite sizes of Cs_4PbBr_6, $CsPbBr_3$ and $PbBr_2$ as 40.6, 22.7 and 29.6 nm, respectively, and the relative weight fractions of Cs_4PbBr_6 and $PbBr_2$ in the white precipitates as 56.9%, and 43.1%, respectively. The corresponding molar fractions of Cs_4PbBr_6 and $PbBr_2$ in the white precipitates are 28.5% and 71.5%, respectively, which gives the molar ratio of Cs_4PbBr_6 to $PbBr_2$ as ~1:3. This result is consistent with the molar ratio of Cs_4PbBr_6 to $PbBr_2$ remained in the brown powders.

For comparison, the XRD pattern of the $CsPbBr_3$ NCs (brown curve) derived from the as-obtained $CsPbBr_3$ powders via ultrasonication of the toluene suspension consisting of OA and OAm is also presented in Fig. 2. The sonication time was 100 min. It is evident that the peaks correspond to the (002), (110), (020), (004), (220), (132) and (224) planes of orthorhombic $CsPbBr_3$ (PDF card#72-7929). Such a result suggests that there are no Cs_4PbBr_6 NCs presented after the ultrasonication. Note that the concentration and sizes of $CsPbBr_3$ NCs/nanoparticles in toluene are dependent on the duration of ultrasonication and the weight fraction of $CsPbBr_3$ powders.

Fig. S4 in Supplementary Information shows the XRD pattern of the $CsPbBr_3$ NCs derived from the as-obtained $CsPbBr_3$ powders after 400-minute ultrasonication and 5-minute centrifugation at 4000 revolution per minute (rpm). The XRD peaks of the obtained $CsPbBr_3$ NCs remain the same as the one (brown curve) in Fig. 2, suggesting that long ultrasonication up to 400 min did not introduce new phases. The $CsPbBr_3$ NCs are orthorhombic (JCPDS card (PDF#72-7929).

The reactions involving the processes of forming the $CsPbBr_3$ powders are illustrated in Fig. 3 and below.

$$CsBr(s) + PbBr_2(s) \rightarrow Cs^+(aq) + Pb^{2+}(aq) + 3Br^-(aq) \quad (1)$$

$$Cs^+(aq) + Pb^{2+}(aq) + 3Br^-(aq) \rightarrow CsPbBr_3(s) \quad (2)$$

$$CsPbBr_3(s) + 3CsBr(s) \rightarrow Cs_4PbBr_6(s) \quad (3)$$

$$Cs4PbBr6(s) + 3PbBr2(s) \xrightarrow{40^\circ C} 4CsPbBr3(s) \quad (4)$$

First, mixing CsBr and $PbBr_2$ powders in DI water leads immediately to the formation of brown $CsPbBr_3$ in water (Fig. S5a and b in Supplementary Information). Note that the solubility of $PbBr_2$ in water is much smaller than CsBr in water. The brown $CsPbBr_3$ precipitates in water, leading to the dissolution of more $PbBr_2$ and the formation of more $CsPbBr_3$ in water. The brown $CsPbBr_3$ then reacts with CsBr in water at room temperature to form white Cs_4PbBr_6 precipitates, which is different from the work reported by Zhai et al. [38] (Fig. S5c in Supplementary Information). The reaction results in the residual of $PbBr_2$ precipitated in water. The heating of the mixture of Cs_4PbBr_6 and $PbBr_2$ at 40°C leads to the formation of $CsPbBr_3$ of orthorhombic structure (Fig. 1b) [37].

According to the reaction of (4), the ratio of the stoichiometric coefficients of Cs_4PbBr_6 to $PbBr_2$ to form $CsPbBr_3$ is 1:3. Such a ratio is in accord with the XRD results in Fig. 2 that the relative weight fractions of Cs_4PbBr_6 and $PbBr_2$ in the white powders, as obtained directly from the water suspension, are 56.9%, and 43.1%, respectively, corresponding to ~1:3 for the ratio of the molar fractions of Cs_4PbBr_6 to $PbBr_2$ in the white powders. This result supports the reaction of (4) indirectly.

Fig. S6 in Supplementary Information presents optical images of the same toluene suspension with $CsPbBr_3$ NCs/particles after three different durations of ultrasonication under white and UV light. It is evident that the concentration of $CsPbBr_3$ NCs/particles increases with the increase of the ultrasonication time. More and more small $CsPbBr_3$ particles were produced during the ultrasonication, which was confirmed by subsequent observation on a Leica SP8 inverted confocal microscope (Fig. S7 in Supplementary Information). According to Fig. S7 in Supplementary Information, the ultrasonication reduced the average size of $CsPbBr_3$ particles from ~35 μm (without ultrasonication) to ~200 nm (after 100 min ultrasonication). The PL spectra (Fig. S8 in Supplementary Information) reveals that increasing the ultrasonication time caused the increase of the PL intensity.

The decrease of the average size of $CsPbBr_3$ particles with the ultrasonication time can be attributed to the force on the $CsPbBr_3$ particles by ultrasonic wave. It is known that the force on a particle due to an ultrasonic wave is proportional to the volume of the particle [39]. The longer the ultrasonication time, the more is the energy absorbed by particles of larger sizes. This trend leads to the disintegration of particles of larger sizes to particles of smaller sizes. Especially, the increase in the energy absorbed in $CsPbBr_3$ particles can cause the nucleation and growth of cracks, leading to the breakage of the particles when the cracks grow through the particles [40] and the production of smaller $CsPbBr_3$ particles. This behavior results in the increase of the concentration of $CsPbBr_3$ particles, which causes the increase in the fluorescence intensity, as shown in Fig. S8 in Supplementary Information.

A simple calculation revealed that the yield of the $CsPbBr_3$ NCs derived from the $CsPbBr_3$ powders is up to 98% (Fig. S1 in Supplementary Information). This is favorable for large-scale production of $CsPbBr_3$ NCs. Also, both the white power in water (Fig. S5c) and brown $CsPbBr_3$ powders in air (Fig. 1b) can be stored longer than half of a year.

The morphologies of the $CsPbBr_3$ NCs/particles were further characterized on a transmission electron microscope. The $CsPbBr_3$ NCs/particles were from a toluene suspension, which was ultrasonicated for 400 min and centrifuged at 1000 rpm for 5 + 1 min, and a toluene suspension, which was ultrasonicated for 400 min and centrifuged at 4000 rpm for 5 min. Fig. S9a in Supplementary Information shows a TEM image of the $CsPbBr_3$ particles. The average size is ~35 nm. The HRTEM image inserted in Fig. S9a exhibits a lattice spacing of 5.64 Å, corresponding to (100) plane of $CsPbBr_3$ [41]. Increasing the centrifugation speed to 4000 rpm, we obtained $CsPbBr_3$ NCs of 3–5 nm in size (Fig. S9b). These results demonstrate that one can use ultrasonication to form $CsPbBr_3$ NCs from the $CsPbBr_3$ powders and the crystalline quality of the $CsPbBr_3$ NCs are comparable to the ones prepared from an

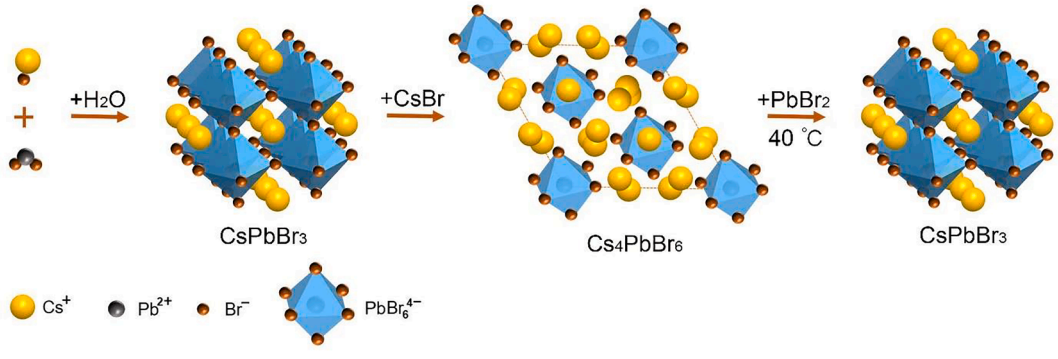

Fig. 3. Crystal model illustrating the formation of orthorhombic $CsPbBr_3$ and hexagonal Cs_4PbBr_6. Step I: reaction between CsBr and $PbBr_2$ in water to form $CsPbBr_3$; step II: reaction of $CsPbBr_3$ with CsBr to form Cs_4PbBr_6; step III reaction of Cs_4PbBr_6 with $PbBr_2$ to form $CsPbBr_3$.

antisolvent process (Fig. S9c). Note that the size of the $CsPbBr_3$ NCs prepared by an antisolvent process is in a range of 8 – 11 nm.

The optical characteristics of the $CsPbBr_3$ NCs prepared by the ultrasonication and antisolvent processes were investigated. Here, the $CsPbBr_3$ NCs prepared by the antisolvent process are used as a benchmark. Fig. 4a and 4d depict the PL and absorption spectra of the $CsPbBr_3$ NCs in toluene, which was ultrasonicated for 100 min without centrifugation. There is a PL peak centered at ~522 nm, and the PLQY is 16.7%. The absorption peak is centered at ~519 nm, and the Stokes shift is ~3 nm. It is interesting to note that the PL spectrum of the $CsPbBr_3$ NCs in the toluene suspension, which was ultrasonicated for 400 min and centrifuged at 4000 rpm for 5 min, exhibits a PL peak at ~493 nm and the PLQY reaches up to 80% (Fig. 4b). The PLQY of 80% is larger than 61.41% of the $CsPbBr_3$ NCs prepared from the antisolvent process (Fig. 4c), and the wavelength of the PL peak is less than ~512 nm of the $CsPbBr_3$ NCs from the antisolvent process. There exists a blue shift, which can be attributed to the size effect of NCs [42] – the smaller the size of a NC, the shorter is the emission wavelength.

Fig. 4e presents the absorption spectrum of the $CsPbBr_3$ NCs in the toluene suspension, which was ultrasonicated for 400 min and centrifuged at 4000 rpm for 5 min. There is a weak absorption peak at ~490 nm, revealing a Stokes shift of ~3 nm. Fig. 4f displays the absorption spectrum of the $CsPbBr_3$ NCs in the toluene suspension, which was prepared from the anti-solvent method, and the Stokes shift is ~3 nm. The results of the Stokes shifts of the three samples indicate a comparable depth of trap states among the three samples [43]. The size variation of the ultrasonication-prepared $CsPbBr_3$ NCs is in accordance with the result reported by Erol et al. [44] that the PL of NCs experiences a blue shift upon a decrease of the NC size. All the results suggest that the $CsPbBr_3$ NCs prepared by the ultrasonication possess superior optical performance to the ones by the antisolvent process.

According to the theory of quantum confinement, the confined ground-state excitonic energy (E_{ex}) as a function of the average size of NCs can be expressed approximately as [42,45,46]

$$E_{ex} = E_g - \frac{13.6}{m_e \varepsilon_r^2} \frac{m_e^* m_h^*}{m_e^* + m_h^*} + \frac{2\pi^2 \hbar^2}{(m_e^* + m_h^*) R_a^2} \tag{5}$$

where E_g is the band gap of bulk semiconductor, ε_r is relative dielectric constant, m_e^* and m_h^* are the reduced masses of electron and hole, respectively, m_e is the mass of electron, $\hbar$ is the Planck constant, and R_a is average size of NCs. The correlation between the excitonic energy and the emission wavelength is

$$E_{ex} = \frac{1240}{\lambda} \tag{6}$$

where$\lambda$is the emission wavelength in the unit of nm. Substituting Eq. (6) in Eq. (5) yields

$$\frac{1240}{\lambda} = E_g - \frac{13.6}{m_e \varepsilon_r^2} \frac{m_e^* m_h^*}{m_e^* + m_h^*} + \frac{2\pi^2 \hbar^2}{(m_e^* + m_h^*) R_a^2} \tag{7}$$

Fig. S10 in Supplementary Information shows the variation of λ^{-1} with R_a^{-2}. It is evident that there exists a linear relation between λ^{-1} and R_a^{-2} in good accord with Eq. (7). The blue shift in the emission wavelength is due to the size effect of the $CsPbBr_3$ NCs.

The time-resolved PL decays of the water-driven $CsPbBr_3$ NCs were studied at a wavelength of 390 nm at room temperature to determine the photogenerated carrier's lifetime of the $CsPbBr_3$ NCs [47]. Fig. 4g-i presents TCSPC curves of the prepared $CsPbBr_3$ NCs. The curves were fitted with a short decay component, τ_1, and a long decay component, τ_2 [47], corresponding to the interactive state (surface) and non-interactive state (core) of the $CsPbBr_3$ NCs, respectively [48–51]. For

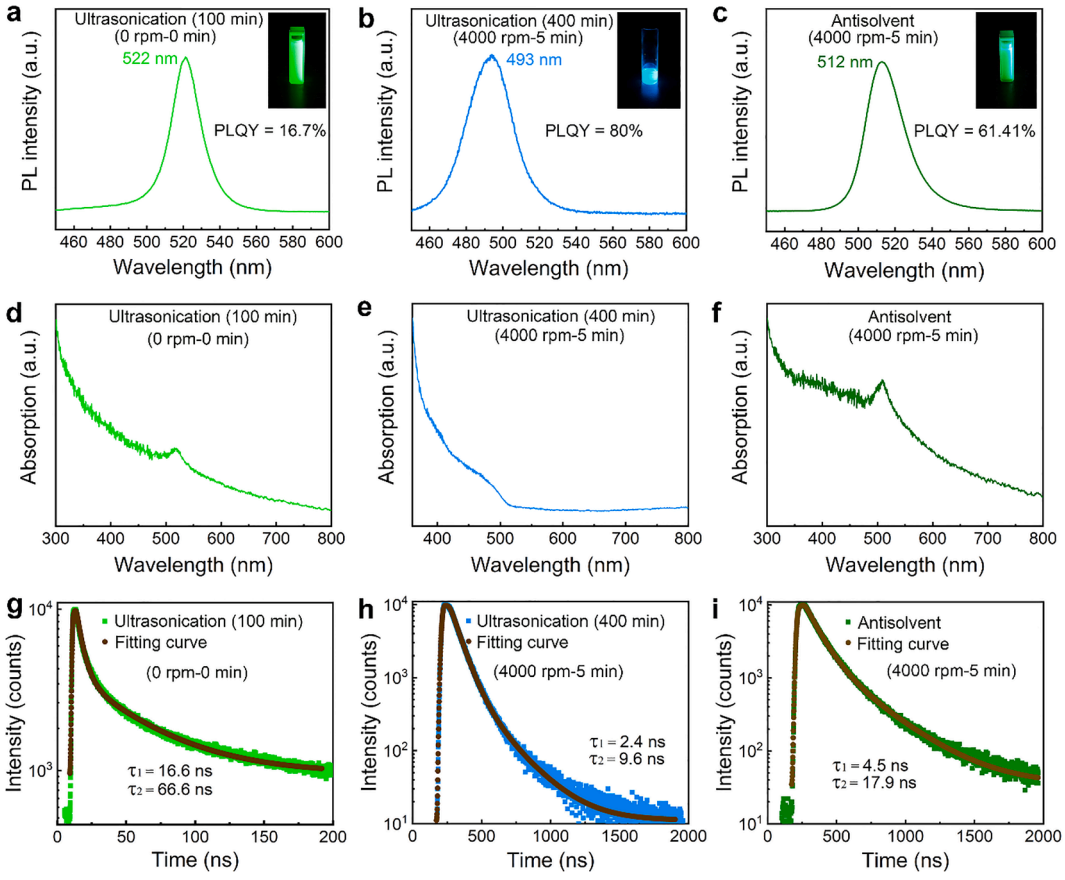

Fig. 4. Optical characteristics of the $CsPbBr_3$ NCs prepared by ultrasonication and antisolvent: (a)-(c) PL spectra, (d)-(f) absorption curves, and (g)-(i) TCSPC curves.

comparison, the fitting curves are also included in Fig. 4g-i. The ratio of the long decay component to the short decay component is 4.01, 4.00 and 3.98 for the $CsPbBr_3$ NCs with 100 min ultrasonication and no centrifugation, with 400 min ultrasonication and 5 min centrifugation at 4000 rpm and from the antisolvent with 5 min centrifugation at 4000 rpm, respectively. There is statistically no difference between the ratios, suggesting almost the same fraction of trapping defect states. Note that the nonradiative decay is determined by trapping defect states [52].

According to Fig. 4g-i, the characteristic time for the long-lived radiative component is 66.6, 9.6 and 17.9 ns for the $CsPbBr_3$ NCs with 100 min ultrasonication and no centrifugation, with 400 min ultrasonication and 5 min centrifugation at 4000 rpm and from the antisolvent with 5 min centrifugation at 4000 rpm, respectively. Such large differences in the characteristic times can be attributed to the effect of the NC size. The larger the NC size, the larger is the characteristic time for the long-lived radiative component. This is because the surface-to-volume ratio decreases rapidly with the increase of NC size, which results in lower surface defect states due to dangling bonds [53] and/or vacancy complexes [54] for NCs of smaller sizes. A lower surface defect state causes the decrease of the short-lived nonradiative component and slows the charge-carrier decay, which may lead to longer PL lifetime [55].

Table S3 in Supplementary Information summaries the optical characteristics of the $CsPbBr_3$ NCs obtained in this work. Table S4 in Supplementary Information lists the PLQYs and the corresponding PL peaks of $CsPbBr_3$ NCs reported in the literature as well as the PLQY and the PL peak obtained in this work. It is evident that the 80% PLQY obtained in this work is comparable or even superior to the results reported in the literature.

The PL stability of the prepared $CsPbBr_3$ NCs without centrifugation was evaluated over a period of 9 days at room temperature under ambient condition. The $CsPbBr_3$ NCs were spin-coated on the surface of indium tin oxide (ITO) substrates. The excitation wavelength of the UV light was 365 nm. Fig. S11 in Supplementary Information shows the PL spectra of the $CsPbBr_3$ NCs, which were made respectively by ultrasonication from the brown powders with the sonication time of 100 min and by the antisolvent method, over a period of 9 days. The PL peak of the $CsPbBr_3$ NCs made by ultrasonication is centered at ~522 nm over the test period, and the PL peak of the $CsPbBr_3$ NCs made by the antisolvent method shifts slightly from ~510 nm to ~514 nm over the same period. The red shift of the PL peak reveals that the $CsPbBr_3$ NCs made by the antisolvent method experienced agglomeration and/or growth over the period likely due to the easy separation of ligands from the surface of the NCs [56]. Such behavior suggests that the $CsPbBr_3$ NCs made by the ultrasonication process are relatively more stable than those made by the antisolvent method. The temporal variation of the corresponding PLQYs of the $CsPbBr_3$ NCs over the same period is shown in Fig. S12 in Supplementary Information. The PLQYs of both the $CsPbBr_3$ NCs exhibit a decreasing trend, and the decay rates are relatively comparable. Note that there is an abnormal drop of the PLQY at the fifth day for the $CsPbBr_3$ NCs made from ultrasonication. The reason for such a drop is unclear.

Using the water-driven $CsPbBr_3$ NCs, we prepared PMMA-NC films on flexible PET plates of $0.80\times6.66\times72.62$ mm^3 in dimensions. The thickness for PMMA-NC films is 30 ± 2.95 μm, as revealed by the optical image of the cross-section of a PMMA-NC film on a PET plate shown in Fig. S13 in Supplementary Information.

Fig. 5a-b shows optical images of the as-prepared films under a UV light (365 nm) without bending (Fig. 5a) and with bending (Fig. 5b). The PL spectra, as shown in Fig. 5c, reveal no PL shift of the $CsPbBr_3$ NCs

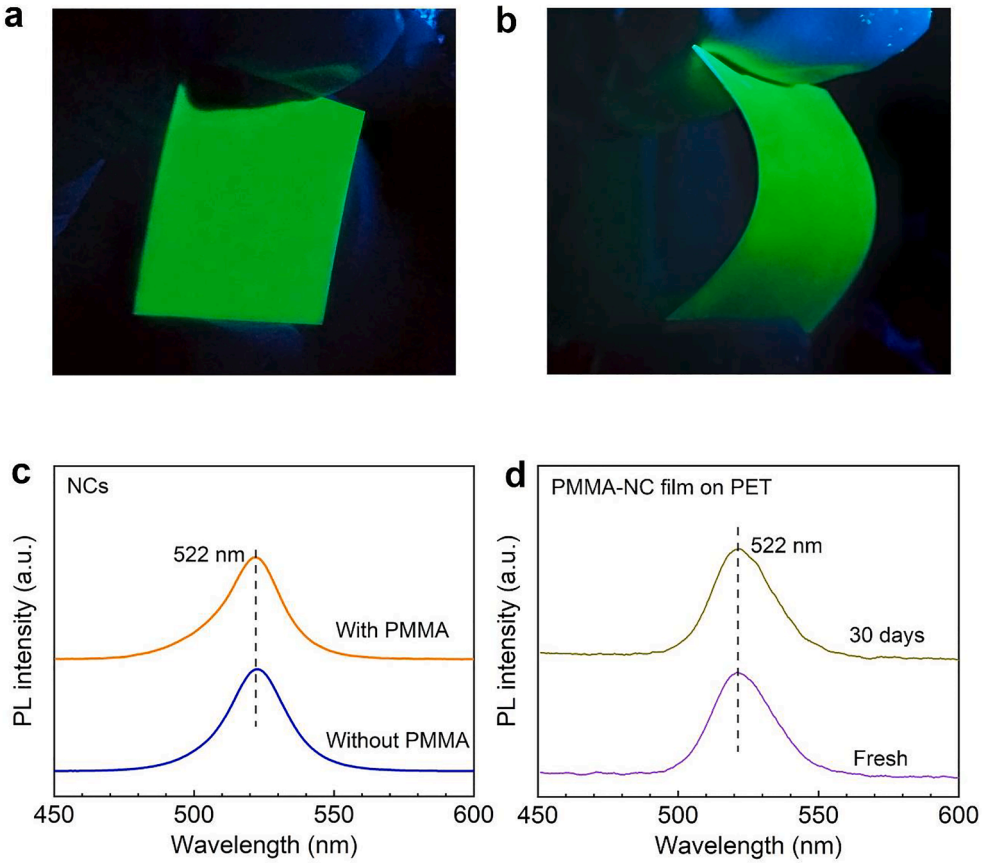

Fig. 5. Optical images of the PMMA-$CsPbBr_3$ NC films (2.5 cm × 2.5 cm) on PET plates under a UV light (365 nm) without bending (a) and with bending (b); (c) PL spectra of $CsPbBr_3$ NCs and PMMA-$CsPbBr_3$ composite, indicating no PL shift, and (d) PL spectra of fresh PMMA-$CsPbBr_3$ NC film on PET and the same film placed in air for 30 days.

after being embedded in PMMA matrix. The PL stability of the PMMA-NC films on PET is depicted in Fig. 5d over a period of 30 days in air (22.0°C and 80% RH). There are no changes in the PL peak and the peak intensity, suggesting excellent PL stability of the PMMA-NC films made from the water-driven $CsPbBr_3$ NCs.

The effect of the bending deformation on the PL characteristics of the PMMA-NC films on PET was examined. Fig. 6a depicts the schematic of the experimental setup for the PL measurement of the bent PMMA-NC films on PET, in which a holder was used to support a reflective optical (RO) probe during the measurement; Fig. S2 in Supplementary Information shows an optical image of a bent PMMA-NC film made from the water-driven green-emitting $CsPbBr_3$ NCs. The PL measurement was conducted at eleven different spatial positions labeled as 1, 2, …, 11 in Fig. 6a. For comparison, we also prepared a set of PMMA-NC films on PET plates of the same geometrical configuration, in which the $CsPbBr_3$ NCs were synthesized by the antisolvent method, and characterized the PL characteristics of the corresponding PMMA-NC films at the same bent state.

Fig. 6b–d and 6e-g present the PL spectra of the PMMA-NC films at the eleven spatial positions, which are denoted as R1, R2, …, R11, at the pristine, bent and "full" recovery states for the films made from the water-driven green-emitting $CsPbBr_3$ NCs and antisolvent-prepared green-emitting $CsPbBr_3$ NCs, respectively. It is evident that there are no observable PL shifts and differences at all the eleven spatial positions between the three different states for the PMMA-NC films made from the water-driven green-emitting $CsPbBr_3$ NCs, which is supported by the excitation-emission contour (mapping) as shown in Fig. S14 (Supplementary Information). The PMMA-NC films made from the water-driven green-emitting $CsPbBr_3$ NCs exhibited excellent bending-endurable PL characteristics and is likely a preferable candidate for flexible display.

For the PMMA-NC films made from antisolvent-prepared green-emitting $CsPbBr_3$ NCs, all the PL peaks at the eleven spatial positions at the pristine state are centered at 523 nm, similar to the PMMA-NC films made from the water-driven green-emitting $CsPbBr_3$ NCs. At the bent state, the PL peaks exhibited red shifts of 1 nm (from 523 nm to 524 nm at R4 and R5) and 2 nm (from 523 nm to 525 nm at R6); at the "full" recovery state, the PL spectra remained the same as the corresponding ones at the bent state. The red shift of the PL peaks reveals the effect of the bending deformation on the PL characteristics of the PMMA-NC films made from the antisolvent-prepared $CsPbBr_3$ NCs, which might hinder the applications of antisolvent-prepared $CsPbBr_3$ NCs in flexible display.

The red shift of the PL peaks likely reveals the change of band gap for the antisolvent-prepared green-emitting $CsPbBr_3$ NCs in the PMMA-NC film at tension state, which can be attributed to the deformation of the $[PbBr_6]^{4-}$ octahedral framework and the variation of Pb-Br-Pb bond angle in $CsPbBr_3$ crystal [57,58]. The change in the spatial positions of atoms in the crystal structure causes the change of band gap [57]. In contrast, the PL peaks of the PMMA-NC films made from the water-driven green-emitting $CsPbBr_3$ NCs remain unchanged at tension for tensile strain less than a threshold value. This behavior might be due to the larger size of the water-driven NCs than the antisolvent-prepared NCs, since the strain dependence of the band gap of nanostructures varies with the dimension of the nanostructures [59].

From the optical images of the bent bilayer structures, such as Fig. S2 in Supplementary Information, the local radius of curvature at the eleven spatial positions are determined and listed in Table S1 in

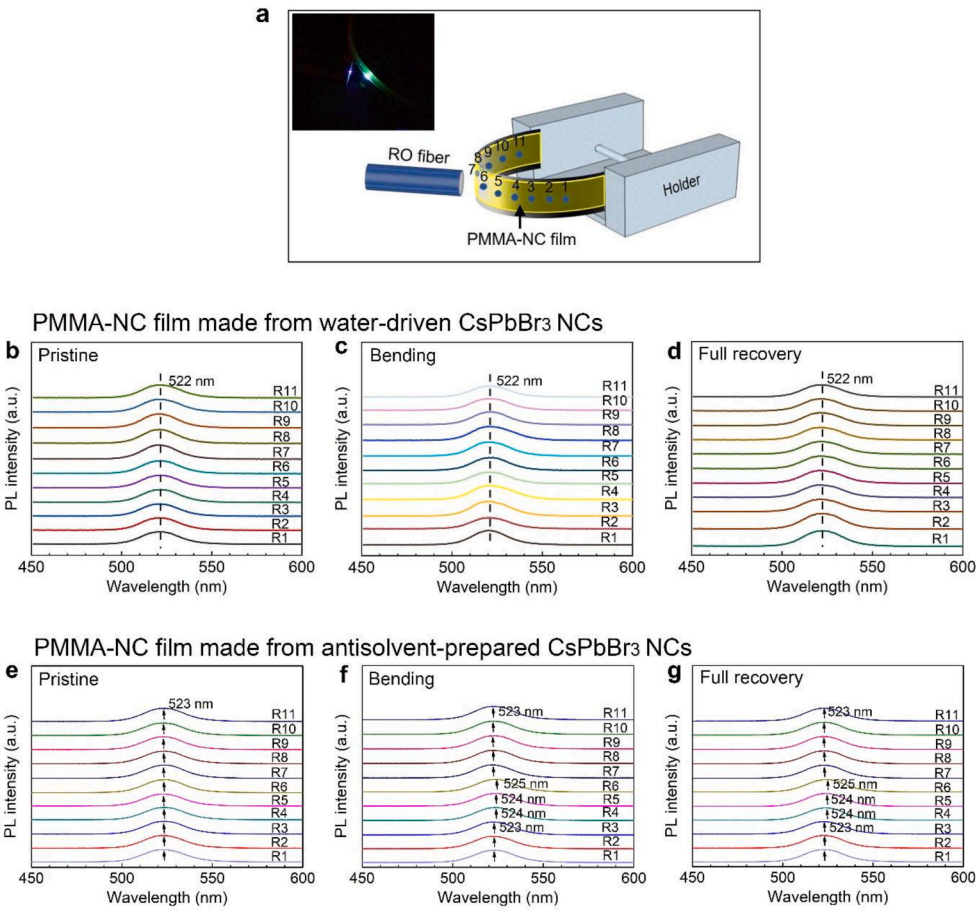

Fig. 6. (a) Schematic of the set up for the PL measurement of the PMMA-NC films at the bent state (Inset: optical image of real objects). The 11 spatial positions (numbered 1, 2, …, 11) are marked for the PL measurement. (b-d) PL spectra of the PMMA-NC film made from water-driven $CsPbBr_3$ NCs, and (e-g) PL spectra of the PMMA-NC film made from water-driven $CsPbBr_3$ NCs.

Supplementary Information, and used to estimate local tensile strain on the PMMA-NC film. According to the bending theory [60], the PMMA-NC films experienced tensile stress/strain, as shown schematically in Fig. 7a. Considering that the thickness of the PMMA-NC film (0.03 mm) is much less than the PET thickness (0.8 mm), the tensile strain on the PMMA-NC film at the bent state is estimated as

$$\varepsilon = y/R = 0.4/R \tag{8}$$

with ε as the tensile strain on the PMMA-NC film, y as the half thickness of the PET plate, and R as the local radius of curvature in the unit of millimeter. Using Eq. (8) and the local radius of curvature, the tensile strains at the eleven spatial positions are calculated and listed in Table S1. The largest tensile strain at the bent state (Fig. S2 in Supplementary Information) is 3.97% at the center of the PMMA-NC film.

It needs to be pointed out that the effect of the PMMA-NC thin film on the spatial distribution of the mechanical strain in the film is negligible. For the NC thin film of 0.03 mm, the largest tensile strain can be estimated to be $(0.4 + 0.03)/R$, i.e. the tensile strain of the NC thin film at the bent state is in a range of 3.97% to 3.97% $(1 + 0.03/0.4)$. It is evident that the strain in the PMMA-NC films can be approximated to be uniform, and the thickness effect on tensile strain is negligible.

To verify the calculation of the local tensile strain, we performed finite element simulation of the bending deformation of the PET plate using commercial software of ANSYS (ANSYS, Inc, Canonsburg, PA). We assumed that the effect of the PMMA-NC film on the PET bending is negligible in the simulation. The Young's modulus, Poisson's ratio and yield stress used in the simulation were 5.2 GPa, 0.405 and 45 MPa, respectively. Fig. 7b shows the simulation result of the deflection profile of the PET plate at the bent state. For comparison, the deflection profile of the bilayer structure at the bent state, which is extracted from the optical image of Fig. S2, is also included in Fig. 7b. It is evident that the numerical results are in good accord with the experimental results. The simulation results reveal that the largest tensile strain is 3.74%, which is quantitatively in agreement with the estimation from the deflection profile of the bilayer structure.

Fig. 7c shows the variation of the shift of the PL peak with the local strain of the PMMA-NC films at the bent state. It is evident that there is no observable shift of the PL peak for the PMMA-NC films made from the water-driven $CsPbBr_3$ NCs for the tensile strain less than 3.97% and for the PMMA-NC films made from the antisolvent-prepared $CsPbBr_3$ NCs for the tensile strain less than or equal to 3.41%.

It is known that PMMA experiences brittle fracture around a tensile strain of 5% at room temperature [61]. Therefore, the deformation of the PMMA-NC films can be approximated as elastic for the largest local tensile strain of 3.97%. The Young's modulus of the PMMA-NC films generally increases with the increase of the concentration of NCs. For a small concentration of NCs, the Young's modulus of the PMMA-NC films is a linear function of the concentration of NCs. Note that there likely exists the effect of surface stress on the elastic modulus of nanocomposites [62]. Here, we use the Youngs modulus of PMMA (3.3 GPa) in the estimation of the stress acting on the PMMA-NC film and obtain a tensile stress of ~13.2 MPa.

Assume that the NCs can be approximated as spherical particles and bonded to the PMMA matrix. Without mismatch strain, the stress concentration, K, can be calculated as [63,64]

$$K = \frac{3}{2}\left[1 - \frac{1-\nu}{2E}\left(\frac{1+\nu}{2E} + \frac{1-\nu'}{2E'}\right)^{-1}\right] \tag{9}$$

with E and E' as the Young's moduli of PMMA and NC, respectively, and ν and ν' as the Poisson's ratios of PMMA and NC, respectively. Thus, the largest tensile stress acting on the NCs is less than 19.8 MPa. For the tensile stress less than or equal to 19.8 MPa on the water-driven green-

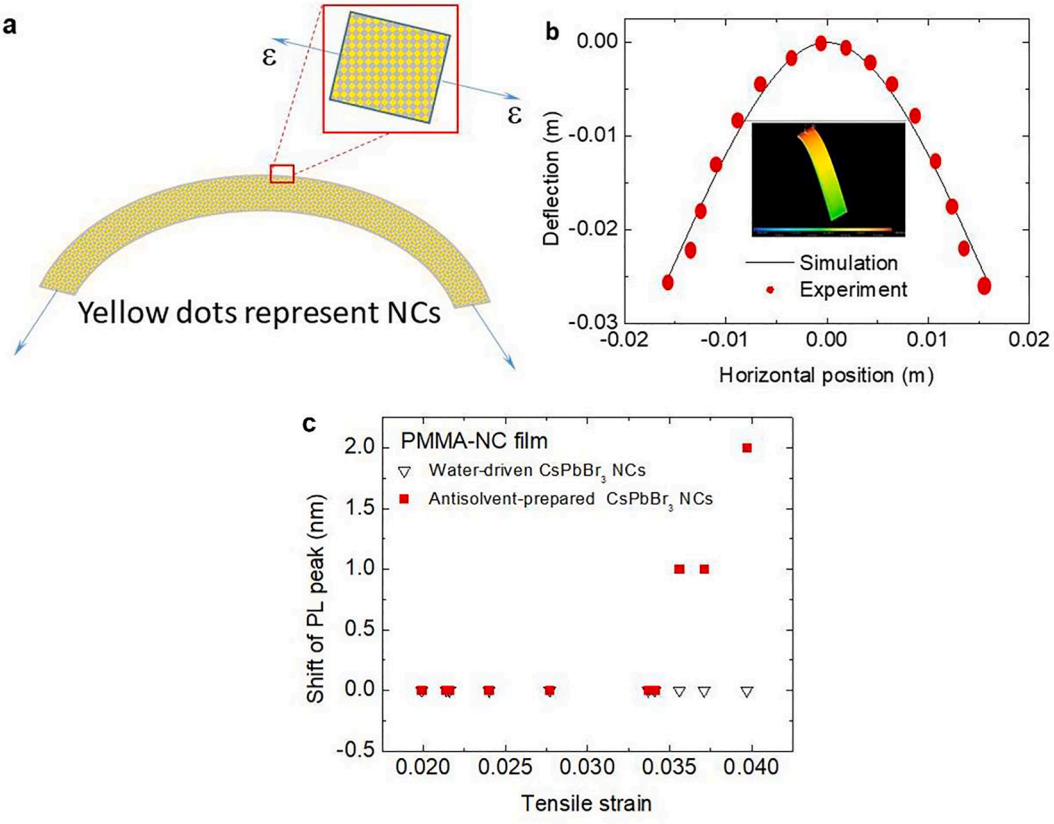

Fig. 7. (a) Schematic of the strain state in the PMMA-NC film for the bent bilayer structure, (b) deflection profile of the bent bilayer structure, and (c) variation of the shift of the PL peak with local tensile strain in the PMMA-NC films.

emitting $CsPbBr_3$ NCs in the PMMA-NC film, there is no observable shift of the PL peak.

The excellent long-term stability and bending-endurable PL characteristic of the PMMA-NC films made from the water-driven green-emitting $CsPbBr_3$ NCs represents a notable progress in the production of semiconductor nanocrystal films (Table S5 in Supplementary Information) and PMMA-NC films (Table S6 in Supplementary Information). These unique feature of the PMMA-NC films can be attributed to the large size of the $CsPbBr_3$ NCs, which leads to a lower level of trap state density [65] and the improvement in the PL stability (Fig. S11 in Supplementary Information). This is because the capture and scattering of the charge carriers through the Shockley–Read–Hall (SRH) recombination during transport is reduced [66].

It is known that the holes and electron defect (trap) states hinder the radiation recombination of electrons and holes and the luminous efficiency of nanocrystals decreases with the increase of the holes and electron defect states [53,68]. For NCs, the surface-to-volume ratio and the fraction of the atoms on surface to those inside increase with the decrease of NC size, which leads to the increases of the fractions of holes and electron defect (trap) states on the surface of NCs with the decrease of NC size [67]. As discussed above, the average size of the green-emitting $CsPbBr_3$ NCs prepared from the anti-solvent method is smaller than those prepared from the ultrasonication. Thus, the green-emitting $CsPbBr_3$ NCs prepared from the anti-solvent method suffer from more fractions of holes and electron defect states, which reduces the luminous efficiency.

We also performed a series of tests to examine the effects of the bending deformation on the crystal structure, TCSPC and absorption behaviors of the PMMA-NC films from the $CsPbBr_3$ NCs prepared by the ultrasonication and antisolvent methods, respectively. Fig. S15 in Supplementary Information depicts the XRD patterns, TCSPC and absorption curves of the PMMA-NC films prior to the bending deformation and after being recovered to the initial-geometrical configuration from the bending deformation. There is no change in the XRD pattern of the corresponding PMMA-NC films (Fig. S15a and b) after the bending deformation, suggesting that the bending deformation did not introduce any changes to the crystal structure of the $CsPbBr_3$ NCs. From the TCSPC curves (Fig. S15c and d), we note that both the short-lived nonradiative component (τ_1) and the long-lived radiative component (τ_2) exhibit slight decreases for both the PMMA-NC films after the bending deformation. However, the changes are much smaller than the corresponding components and are negligible. There is no significant change in the lifetime for both the PMMA-NC films. According to Fig. S15e and f, there is a red shift of 1 nm for the absorption of the PMMA-NC films from the $CsPbBr_3$ NCs prepared by the anti-solvent method, and there is no shift for the absorption of the PMMA-NC films from the $CsPbBr_3$ NCs prepared by the ultrasonication. Such a result is in good accord with the dependence of the PL peak on the bending deformation, as shown in Fig. 6.

4. Conclusion

In summary, we have developed a facile route for the green synthesis of microsized $CsPbBr_3$ crystals for the first time without conventional, harmful orgonic solvent in precursor solutions, such as N,N-dimethylformamide and dimethyl sulfoxide. The chemical reaction between CsBr and $PbBr_2$ in DI water leads to the formation of Cs_4PbBr_6 white precipitates, which then react with $PbBr_2$ to form $CsPbBr_3$ powders, as supported by XRD. The ultrasonication and/or centrifugation of the $CsPbBr_3$ powders in toluene with a small amount of oleic acid and oleylamine reduce the size of the $CsPbBr_3$ powders, resulting in $CsPbBr_3$ NCs of nanosizes.

The TEM analysis of the morphologies of the $CsPbBr_3$ NCs illustrates that one can use the combination of ultrasonication and centrifugation to derive blue-emitting (~493 nm) $CsPbBr_3$ NCs of ~3 nm in size from the $CsPbBr_3$ powders. It is the ultrasonic wave that interacts with the $CsPbBr_3$ powders and causes the disintegration of the $CsPbBr_3$ powders to form $CsPbBr_3$ NCs. The $CsPbBr_3$ NCs prepared by the ultrasonication possessed slightly fewer surface defects than those by the antisolvent method and exhibited better long-term PL stability than those by the antisolvent method. The PMMA-NC films prepared from the water-driven $CsPbBr_3$ NCs exhibited excellent bending-endurable characteristic without the PL shift for the local radius of curvature larger than or equal to 10.78 mm, corresponding to a tensile stress of ~19.8 MPa.

The method developed in this work provides a green technique to synthesize microsized $CsPbBr_3$ crystals. Such a method opens a new avenue to potentially produce inorganic halide perovskite powders without the use of harmful organic solvents, which will further benefit for the eco-friendly manufacture of anti-distortion backlight films for flexible LCD applications.

Declaration of Competing Interest

The authors declare that they have no known competing financial interests or personal relationships that could have appeared to influence the work reported in this paper.

Acknowledgements

FY is grateful for the support by the NSF through the grant no. CMMI-1854554, monitored by Drs. Khershed Cooper and Thomas Francis Kuech, and CBET- 2018411 monitored by Dr. Nora F Savage. The authors thank Dr. J. Pham and Ms. Z.Y. Cai (Materials Program, Department of Chemical and Materials Engineering, University of Kentucky, Lexington, KY 40506) for the imaging of the $CsPbBr_3$ NCs/powders on a Leica SP8 inverted confocal microscope.

Appendix A. Supplementary data

Supplementary data to this article can be found online at https://doi.org/10.1016/j.cej.2021.131456.

References

[1] X. Dai, Z. Zhang, Y. Jin, Y. Niu, H. Cao, X. Liang, L. Chen, J. Wang, X. Peng, Solution-processed, high-performance light-emitting diodes based on quantum dots, Nature 515 (7525) (2014) 96–99.
[2] A. Rogach, N. Gaponik, J. Lupton, C. Bertoni, D. Gallardo, S. Dunn, N. LiPira, M. Paderi, P. Repetto, S. Romanov, C. O'Dwyer, C. SotomayorTorres, A. Eychmüller, Light-emitting diodes with semiconductor nanocrystals, Angew. Chem. Int. Ed. 47 (35) (2008) 6538–6549.
[3] K. Bourzac, Quantum dots go on display, Nature 493 (7432) (2013) 283, 283.
[4] F. Gao, W. Yang, X. Liu, Y. Li, W. Liu, H. Xu, Y. Liu, Highly stable and luminescent silica-coated perovskite quantum dots at nanoscale-particle level via nonpolar solvent synthesis, Chem. Eng. J. 407 (2021), 128001.
[5] E.H. Sargent, Colloidal quantum dot solar cells, Nat. Photonics 6 (3) (2012) 133–135.
[6] G.S. Selopal, H. Zhao, Z.M. Wang, F. Rosei, Core/Shell quantum dots solar cells, Adv. Funct. Mater. 30 (13) (2020) 1908762, https://doi.org/10.1002/adfm.v30.1310.1002/adfm.201908762.
[7] X. Michalet, F.F. Pinaud, L.A. Bentolila, J.M. Tsay, S. Doose, J.J. Li, G. Sundaresan, A. Wu, S. Gambhir, S. Weiss, Quantum dots for live cells, in vivo imaging, and diagnostics, Science 307 (2005) 538–544.
[8] M.-K. So, C. Xu, A.M. Loening, S.S. Gambhir, J. Rao, Self-illuminating quantum dot conjugates for in vivo imaging, Nat. Biotechnol. 24 (3) (2006) 339–343.
[9] F. Zhang, H. Zhong, C. Chen, X.-G. Wu, X. Hu, H. Huang, J. Han, B. Zou, Y. Dong, Brightly luminescent and color-tunable colloidal $CH_3NH_3PbX_3$ (X= Br, I, Cl) quantum dots: potential alternatives for display technology, ACS Nano 9 (2015) 4533–4542.
[10] Y. Chen, J. Vela, H. Htoon, J.L. Casson, D.J. Werder, D.A. Bussian, V.I. Klimov, J. A. Hollingsworth, "Giant" multishell CdSe nanocrystal quantum dots with suppressed blinking, J. Am. Chem. Soc. 130 (15) (2008) 5026–5027.
[11] Z. Cao, Y. Shu, H. Qin, B. Su, X. Peng, Quantum dots with highly efficient, stable, and multicolor electrochemiluminescence, ACS Cent. Sci. 6 (7) (2020) 1129–1137.
[12] W. Yang, L. Fei, F. Gao, W. Liu, H. Xu, L. Yang, Y. Liu, Thermal polymerization synthesis of CsPbBr 3 perovskite-quantum-dots@ copolymer composite: towards long-term stability and optical phosphor application, Chem. Eng. J. 387 (2020), 124180.
[13] Y.i. Wei, Z. Cheng, J. Lin, An overview on enhancing the stability of lead halide perovskite quantum dots and their applications in phosphor-converted LEDs, Chem. Soc. Rev. 48 (1) (2019) 310–350.

[14] W. Yang, F. Gao, Y. Qiu, W. Liu, H. Xu, L. Yang, Y. Liu, CsPbBr 3-Quantum-Dots/Polystyrene@silica hybrid microsphere structures with significantly improved stability for white LEDs, Adv. Opt. Mater. 7 (2019) 1900546.

[15] M.V. Kovalenko, L. Protesescu, M.I. Bodnarchuk, Properties and potential optoelectronic applications of lead halide perovskite nanocrystals, Science 358 (6364) (2017) 745–750.

[16] C. Sun, Y.u. Zhang, C. Ruan, C. Yin, X. Wang, Y. Wang, W.W. Yu, Efficient and stable white LEDs with silica-coated inorganic perovskite quantum dots, Adv. Mater. 28 (45) (2016) 10088–10094.

[17] Q.A. Akkerman, G. Rainò, M.V. Kovalenko, L. Manna, Genesis, challenges and opportunities for colloidal lead halide perovskite nanocrystals, Nat. Mater. 17 (5) (2018) 394–405.

[18] Y.u. Tong, E. Bladt, M.F. Aygüler, A. Manzi, K.Z. Milowska, V.A. Hintermayr, P. Docampo, S. Bals, A.S. Urban, L. Polavarapu, J. Feldmann, Highly luminescent cesium lead halide perovskite nanocrystals with tunable composition and thickness by ultrasonication, Angew. Chem. Int. Ed. 55 (44) (2016) 13887–13892.

[19] H.e. Huang, Q.i. Xue, B. Chen, Y. Xiong, J. Schneider, C. Zhi, H. Zhong, A. L. Rogach, Top-down fabrication of stable methylammonium lead halide perovskite nanocrystals by employing a mixture of ligands as coordinating solvents, Angew. Chem. 129 (32) (2017) 9699–9704.

[20] Y. Wang, J. He, H. Chen, J. Chen, R. Zhu, P. Ma, A. Towers, Y. Lin, A.J. Gesquiere, S.-T. Wu, Y. Dong, Ultrastable, highly luminescent organic–inorganic perovskite–polymer composite films, Adv. Mater. 28 (48) (2016) 10710–10717.

[21] M. Imran, V. Caligiuri, M. Wang, L. Goldoni, M. Prato, R. Krahne, L. De Trizio, L. Manna, Benzoyl halides as alternative precursors for the colloidal synthesis of lead-based halide perovskite nanocrystals, J. Am. Chem. Soc. 140 (7) (2018) 2656–2664.

[22] X. Wang, Z. Bao, Y.-C. Chang, R.-S. Liu, Perovskite quantum dots for application in high color gamut backlighting display of light-emitting diodes, ACS Energy Lett. 5 (11) (2020) 3374–3396.

[23] E. Jang, S. Jun, H. Jang, J. Lim, B. Kim, Y. Kim, White-light-emitting diodes with quantum dot color converters for display backlights, Adv. Mater. 22 (28) (2010) 3076–3080.

[24] X. Li, Y. Luo, M.V. Holt, Z. Cai, D.P. Fenning, Residual nanoscale strain in cesium lead bromide perovskite reduces stability and shifts local luminescence, Chem. Mater. 31 (8) (2019) 2778–2785.

[25] H. Ding, M. Liu, N. Pan, Y. Dong, Y. Lin, T. Li, J. Zhao, Z. Luo, Y.i. Luo, X. Wang, Lattice disorder-engineered energy splitting between bright and dark excitons in CsPbBr 3 quantum wires, The Journal of Physical Chemistry Letters 10 (6) (2019) 1355–1360.

[26] X. Yin, C.S. Tang, M.A. Majidi, P. Ren, L.e. Wang, P. Yang, C. Diao, X. Yu, M.B. H. Breese, A.T.S. Wee, J. Wang, A. Rusydi, Modulation of manganite nanofilm properties mediated by strong influence of strontium titanate excitons, ACS Appl. Mater. Interfaces 10 (41) (2018) 35563–35570.

[27] V. Naresh, B.H. Kim, N. Lee, Synthesis of $CsPbX_3$ (X= Cl/Br, Br, and Br/I)@ SiO_2/PMMA composite films as color-conversion materials for achieving tunable multi-color and white light emission, Nano Res. 14 (4) (2021) 1187–1194.

[28] G. Dai, L. Wang, S. Cheng, Y.u. Chen, X. Liu, L. Deng, H. Zhong, Perovskite quantum dots based optical Fabry-Pérot pressuresensor, ACS Photonics 7 (9) (2020) 2390–2394.

[29] L. Protesescu, S. Yakunin, M.I. Bodnarchuk, F. Krieg, R. Caputo, C.H. Hendon, R. X. Yang, A. Walsh, M.V. Kovalenko, Nanocrystals of cesium lead halide perovskites ($CsPbX_3$, X= Cl, Br, and I): novel optoelectronic materials showing bright emission with wide color gamut, Nano Lett. 15 (2015) 3692–3696.

[30] X. Li, Y. Wu, S. Zhang, B. Cai, Y. Gu, J. Song, H. Zeng, $CsPbX_3$ quantum dots for lighting and displays: room-temperature synthesis, photoluminescence superiorities, underlying origins and white light-emitting diodes, Adv. Funct. Mater. 26 (2016) 2435–2445.

[31] Z. Li, Q. Hu, Z. Tan, Y. Yang, M. Leng, X. Liu, C. Ge, G. Niu, J. Tang, Aqueous synthesis of lead halide perovskite nanocrystals with high water stability and bright photoluminescence, ACS Appl. Mater. Interfaces 10 (50) (2018) 43915–43922.

[32] N.-G. Park, Green solvent for perovskite solar cell production, Nat. Sustainability 4 (2020) 1–2.

[33] X. Cao, G. Zhang, L. Jiang, Y. Cai, Y. Gao, W. Yang, X. He, Q. Zeng, G. Xing, Y.i. Jia, J. Wei, Water, a green solvent for fabrication of high-quality CsPbBr 3 films for efficient solar cells, ACS Appl. Mater. Interfaces 12 (5) (2020) 5925–5931.

[34] X. Chen, F. Zhang, Y. Ge, L. Shi, S. Huang, J. Tang, Z. Lv, L. Zhang, B. Zou, H. Zhong, Centimeter-sized Cs_4PbBr 6 crystals with embedded $CsPbB_r3$ nanocrystals showing superior photoluminescence: nonstoichiometry induced transformation and light-emitting applications, Adv. Funct. Mater. 28 (2018) 1706567.

[35] L.N. Quan, R. Quintero-Bermudez, O. Voznyy, G. Walters, A. Jain, J.Z. Fan, X. Zheng, Z. Yang, E.H. Sargent, Highly emissive green perovskite nanocrystals in a solid state crystalline matrix, Adv. Mater. 29 (2017) 1605945.

[36] S. Park, M.N. An, G. Almeida, F. Palazon, D. Spirito, R. Krahne, Z. Dang, L. De Trizio, L. Manna, $CsPbX_3/SiO_x$ (X= Cl, Br, I) monoliths prepared via a novel sol–gel route starting from Cs_4PbX_6 nanocrystals, Nanoscale 11 (40) (2019) 18739–18745.

[37] Q.A. Akkerman, S. Park, E. Radicchi, F. Nunzi, E. Mosconi, F. De Angelis, R. Brescia, P. Rastogi, M. Prato, L. Manna, Nearly monodisperse insulator Cs_4PbX_6 (X= Cl, Br, I) nanocrystals, their mixed halide compositions, and their transformation into $CsPbX_3$ nanocrystals, Nano Lett. 17 (3) (2017) 1924–1930.

[38] W. Zhai, J. Lin, Q. Li, K. Zheng, Y. Huang, Y. Yao, X. He, L. Li, C. Yu, C. Liu, Y.i. Fang, Z. Liu, C. Tang, Solvothermal synthesis of ultrathin cesium lead halide perovskite nanoplatelets with tunable lateral sizes and their reversible transformation into Cs_4PbBr 6 nanocrystals, Chem. Mater. 30 (11) (2018) 3714–3721.

[39] S.M. Woodside, B.D. Bowen, J.M. Piret, Measurement of ultrasonic forces for particle–liquid separations, AIChE J. 43 (7) (1997) 1727–1736.

[40] F. Yu, Particle breakage in granular soils: a review, Part. Sci. Technol. 39 (2019) 1–10.

[41] X. Tang, W. Chen, D. Wu, A. Gao, G. Li, J. Sun, K. Yi, Z. Wang, G. Pang, H. Yang, In situ growth of all-inorganic perovskite single crystal arrays on electron transport layer, Adv. Sci. 7 (2020) 1902767.

[42] Z. Fu, Y. Cui, S. Zhang, J. Chen, D. Yu, S. Zhang, L. Niu, J. Jiang, Study on the quantum confinement effect on ultraviolet photoluminescence of crystalline ZnO nanoparticles with nearly uniform size, Appl. Phys. Lett. 90 (2007), 263113.

[43] E.M. Janke, N.E. Williams, C. She, D. Zherebetskyy, M.H. Hudson, L. Wang, D. J. Gosztola, R.D. Schaller, B. Lee, C. Sun, Origin of broad emission spectra in InP quantum dots: Contributions from structural and electronic disorder, J. Am. Chem. Soc. 140 (2018) 15791–15803.

[44] E. Erol, O. Kıbrıslı, M.Ç. Ersundu, A.E. Ersundu, Size-controlled emission of long-time durable CsPbBr 3 perovskite quantum dots embedded tellurite glass nanocomposites, Chem. Eng. J. 401 (2020), 126053.

[45] E. Hanamura, Very large optical nonlinearity of semiconductor microcrystallites, Physical Review B 37 (3) (1988) 1273–1279.

[46] F. Yang, Size effect on the bandgap change of quantum dots: Thermomechanical deformation, Phys. Lett. A 401 (2021) 127346, https://doi.org/10.1016/j.physleta.2021.127346.

[47] J. Huang, T. Lei, M. Siron, Y.e. Zhang, S. Yu, F. Seeler, A. Dehestani, L.N. Quan, K. Schierle-Arndt, P. Yang, Lead-free cesium europium halide perovskite nanocrystals, Nano Lett. 20 (5) (2020) 3734–3739.

[48] B.G. Yacobi, D.B. Holt, Cathodoluminescence microscopy of inorganic solids, Springer, New York, 1990, pp. 55–88.

[49] D. Shi, V. Adinolfi, R. Comin, M. Yuan, E. Alarousu, A. Buin, Y. Chen, S. Hoogland, A. Rothenberger, K. Katsiev, Y. Losovyj, X. Zhang, P.A. Dowben, O.F. Mohammed, E.H. Sargent, O.M. Bakr, Low trap-state density and long carrier diffusion in organolead trihalide perovskite single crystals, Science 347 (6221) (2015) 519–522.

[50] J.T. DuBose, P.V. Kamat, Surface Chemistry Matters. How ligands influence excited state interactions between CsPbBr 3 and Methyl Viologen, The Journal of Physical Chemistry C 124 (24) (2020) 12990–12998.

[51] Y.J. Yoon, Y.S. Shin, C.B. Park, J.G. Son, J.W. Kim, H.S. Kim, W. Lee, J. Heo, G.-H. Kim, J.Y. Kim, Origin of the luminescence spectra width in perovskite nanocrystals with surface passivation, Nanoscale 12 (42) (2020) 21695–21702.

[52] Y.D. Glinka, T.V. Shahbazyan, I.E. Perakis, N.H. Tolk, X. Liu, Y. Sasaki, J. K. Furdyna, Ultrafast dynamics of interfacial electric fields in semiconductor heterostructures monitored by pump-probe second-harmonic generation, Appl. Phys. Lett. 81 (20) (2002) 3717–3719.

[53] H. Fu, A. Zunger, InP quantum dots: Electronic structure, surface effects, and the redshifted emission, Physical Review B 56 (1997) 1496–1508.

[54] Ü. Özgür, Y.I. Alivov, C. Liu, A. Teke, M. Reshchikov, S. Doğan, V. Avrutin, S.-J. Cho, Morkoç, A comprehensive review of ZnO materials and devices, J. Appl. Phys. 98 (2005), 041301.

[55] T. Kirchartz, T. Markvart, U. Rau, D.A. Egger, Impact of small phonon energies on the charge-carrier lifetimes in metal-halide perovskites, The Journal of Physical Chemistry Letters 9 (5) (2018) 939–946.

[56] J. Chen, D. Liu, M.J. Al-Marri, L. Nuuttila, H. Lehtivuori, K. Zheng, Photo-stability of $CsPbBr_3$ perovskite quantum dots for optoelectronic application, Sci. China Mater. 59 (9) (2016) 719–727.

[57] Q. Tu, I. Spanopoulos, S. Hao, C. Wolverton, M.G. Kanatzidis, G.S. Shekhawat, V. P. Dravid, Probing strain-induced band gap modulation in 2D hybrid organic–inorganic perovskites, ACS Energy Lett. 4 (3) (2019) 796–802.

[58] D.B. Kim, J.W. Lee, Y.S. Cho, Anisotropic in situ strain-engineered halide perovskites for high mechanical flexibility, Adv. Funct. Mater. 31 (2021) 2007131.

[59] S. Yang, D. Prendergast, J.B. Neaton, Strain-induced band gap modification in coherent core/shell nanostructures, Nano Lett. 10 (8) (2010) 3156–3162.

[60] S.P. Timoshenko, S. Woinowsky-Krieger, Theory of plates and shells, McGraw-Hill, New York, 1959.

[61] A.A. Abdel-Wahab, S. Ataya, V.V. Silberschmidt, Temperature-dependent mechanical behaviour of PMMA: Experimental analysis and modelling, Polym. Test. 58 (2017) 86–95.

[62] F. Yang, Effect of interfacial stresses on the elastic behavior of nanocomposite materials, J. Appl. Phys. 99 (2006), 054306.

[63] S. Yin, Z. Zhao, W. Luan, F. Yang, Optical response of a quantum dot–epoxy resin composite: effect of tensile strain, RSC Adv. 6 (22) (2016) 18126–18133.

[64] P.C. Paris, T. Palin-Luc, H. Tada, N. Saintier, Stresses and crack tip stress intensity factors around spherical and cylindrical voids and inclusions of differing elastic properties and with misfit sizes, Proceedings Int. Crack Path, ESIS Ed., Vicenza, Italy (2009) 23-25.

[65] S. Huang, Z. Li, B.o. Wang, N. Zhu, C. Zhang, L. Kong, Q.i. Zhang, A. Shan, L. Li, Morphology evolution and degradation of CsPbBr 3 nanocrystals under blue light-emitting diode illumination, ACS Appl. Mater. Interfaces 9 (8) (2017) 7249–7258.

[66] K. Wang, C. Wu, Y. Hou, D. Yang, S. Priya, Monocrystalline perovskite wafers/thin films for photovoltaic and transistor applications, J. Mater. Chem. A 7 (43) (2019) 24661–24690.

[67] S.V. Kilina, P.K. Tamukong, D.S. Kilin, Surface chemistry of semiconducting quantum dots: theoretical perspectives, Acc. Chem. Res. 49 (10) (2016) 2127–2135.

[68] B.P. Bloom, L.-B. Zhao, Y. Wang, D.H. Waldeck, R. Liu, P. Zhang, D.N. Beratan, Ligand-induced changes in the characteristic size-dependent electronic energies of CdSe nanocrystals, The Journal of Physical Chemistry C 117 (43) (2013) 22401–22411.